

NGC 6240: A triple nucleus system in the advanced or final state of merging[★]

W. Kollatschny¹, P. M. Weilbacher², M. W. Ochmann¹, D. Chelouche³, A. Monreal-Ibero^{4,5},
R. Bacon⁶, and T. Contini⁷

¹ Institut für Astrophysik, Universität Göttingen, Friedrich-Hund Platz 1, 37077 Göttingen, Germany
e-mail: wkollat@astro.physik.uni-goettingen.de

² Leibniz-Institut für Astrophysik Potsdam (AIP), An der Sternwarte 16, 14482 Potsdam, Germany

³ Physics Department and the Haifa Research Center for Theoretical Physics and Astrophysics, University of Haifa, Haifa 3498838, Israel

⁴ Instituto de Astrofísica de Canarias (IAC), 38205 La Laguna, Tenerife, Spain

⁵ Universidad de La Laguna, Dpto. Astrofísica, 38206 La Laguna, Tenerife, Spain

⁶ Univ. Lyon, Univ. Lyon1, ENS de Lyon, CNRS, Centre de Recherche Astrophysique de Lyon UMR5574, 69230 Saint-Genis-Laval, France

⁷ Institut de Recherche en Astrophysique et Planétologie (IRAP), Université de Toulouse, CNRS, UPS, 31400 Toulouse, France

Received 21 August 2019 / Accepted 27 October 2019

ABSTRACT

Aims. NGC 6240 is a well-studied nearby galaxy system in the process of merging. Based on optical, X-ray, and radio observations, it is thought to harbor two active nuclei. We carried out a detailed optical 3D spectroscopic study to investigate the inner region of this system in connection with existing MERLIN and VLBA data.

Methods. We observed NGC 6240 with very high spatial resolution using the MUSE instrument in the Narrow-Field Mode with the four-laser GALACSI adaptive optics system on the ESO VLT under seeing conditions of 0".49. Our 3D spectra cover the wavelength range from 4725 to 9350 Å at a spatial resolution of ~75 mas.

Results. We report the discovery of three nuclei in the final state of merging within a region of only 1 kpc in the NGC 6240 system. Thanks to MUSE we are able to show that the formerly unresolved southern component actually consists of two distinct nuclei separated by only 198 pc. In combination with *Gaia* data we reach an absolute positional accuracy of only 30 mas that is essential to compare optical spectra with MERLIN and VLBA radio positions.

Conclusions. The verification and detailed study of a system with three nuclei, two of which are active and each with a mass in excess of $9 \times 10^7 M_{\odot}$, is of great importance for the understanding of hierarchical galaxy formation via merging processes since multiple mergers lead to a faster evolution of massive galaxies in comparison to binary mergers. So far it has been suggested that the formation of galactic nuclei with multiple supermassive black holes (SMBHs) is expected to be rare in the local universe. Triple massive black hole systems might be of fundamental importance for the coalescence of massive black hole binaries in less than a Hubble time leading to the loudest sources of gravitational waves in the millihertz regime.

Key words. galaxies: active – galaxies: interactions – instrumentation: high angular resolution – galaxies: individual: NGC 6240 – galaxies: nuclei

1. Introduction

It is generally accepted that all massive galaxies host supermassive black holes (SMBHs) in their centers (Kormendy & Ho 2013) and that mergers of two galaxies lead to the formation of black hole binaries. These binaries might evolve into single or double active galactic nuclei (AGN) if their nuclei are accreting gas (Begelman et al. 1980). If the binary lifetime exceeds the typical time between mergers, triple black hole systems may form (Hoffman & Loeb 2007). Of these systems, the most interesting ones are those in an advanced state of merging (i.e., those with the smallest distances between their SMBHs). The closest known optical or infrared distances of two nuclei correspond to a projected separation of ~one kiloparsec, except for only one example, MCG+02-21-013, with a projected separation of

300 pc (see Table 1 in Koss et al. 2018). Arp 220, which is the nearest ultraluminous infrared galaxy (ULIRG), has two near-IR nuclei at a separation of 330 pc (Genzel et al. 2001, and references therein). The detection of another close-separation binary quasar has been reported recently (Goulding et al. 2019). The nuclei in SDSS J1010+1413 are separated by 430 pc only.

Here we present high spatial resolution observations of the nearby merging galaxy system NGC 6240 obtained with the MUSE instrument at the ESO VLT. NGC 6240 is one of the nearest ULIRGs (Genzel & Cesarsky 2000). It is at the faint limit of the ULIRG class with respect to its far-IR luminosity (Wright et al. 1984). NGC 6240 belongs to the class of merging systems where the galaxies are separated by less than 10 kpc based on optical and IR images (Koss et al. 2018). It is the merging system with the second smallest separation between the two components in the list of Koss et al. (2018), corresponding to a projected separation of 900 pc between its northern and southern components. It has been proposed that NGC 6240 is a merger of two massive

* The reduced datacubes are only available at the CDS via anonymous ftp to cdsarc.u-strasbg.fr (130.79.128.5) or via <http://cdsarc.u-strasbg.fr/viz-bin/cat/J/A+A/633/A79>

disk galaxies (e.g., Fosbury & Wall 1979; Engel et al. 2010 and references therein).

NGC 6240 has been the subject of numerous studies. Based on radio observations with MERLIN and VLBA (Gallimore & Beswick 2004) and X-ray observations with *Chandra* (Komossa et al. 2003), it has been claimed that NGC 6240 hosts a pair of AGN. However, to date the exact location of the two active nuclei is not accurately known as the two radio positions are separated by 1.51 arcsec (e.g., Max et al. 2007), while the two brightest near-IR or optical spots are separated by 1.8 arcsec.

There are very few other cases of merging systems where the two nuclei are separated by less than 10 kpc and at the same time show Seyfert characteristics (e.g., Satyapal et al. 2017, their Table 8). Among those double nucleus Seyfert galaxies are objects like Mrk 266 (Kollatschny & Fricke 1984; Kollatschny & Kowatsch 1998; Mazzarella et al. 2012) and Mrk 739 (Netzer et al. 1987) that have been studied in detail for many years.

NGC 6240 has a mean redshift of $z = 0.02448$ (Downes et al. 1993) corresponding to 7339 km s^{-1} . Throughout this paper we assume Λ cold dark matter cosmology with a Hubble constant of $H_0 = 73 \text{ km s}^{-1} \text{ Mpc}^{-1}$, $\Omega_M = 0.27$, and $\Omega_\Lambda = 0.73$. Following the cosmological calculator by Wright (2006) this results in a luminosity distance of 102 Mpc with a scale of 1 arcsec = 473 pc.

2. Observations and data reduction

2.1. MUSE observations

We observed NGC 6240 on April 22, 2018, as part of the commissioning run of the MUSE (Multi Unit Spectroscopic Explorer, Bacon et al. 2010, 2014) instrument in the Narrow-Field Mode (NFM) with the four-laser adaptive optics system of ESO's Very Large Telescope (VLT) unit telescope four (Yepun). We used the peak of the southern emission region S1 (in the *H* band) as an on-axis tip-tilt object, centered by the large-scale pick-off. We exposed four 500 s science exposures on the center of NGC 6240 and another 500 s exposure on an offset sky field. We rotated 90 deg between each on-target exposure. Spatial offsets of about $1''.5$ resulted in significantly larger coverage of $\sim 11''.5 \times 11''.5$ with some gaps at the field edges. The NFM covers a field of $7''.5 \times 7''.5$ on the sky, sampled at about 25 mas. A seeing of $0''.49 \pm 0''.07$ was measured with the differential image motion monitor (DIMM) at the time of observations. The target was observed at an airmass of 1.13. The wavelength range coverage is 4725 to 9350 Å, with a spectral resolution of about 2.5 Å. The spectra are sampled at 1.25 Å in dispersion direction and $0''.0253$ in spatial direction. There is a gap in the spectrum between 5780 and 6050 Å because of the sodium laser-guide system.

2.2. Data reduction

We reduced the data using the MUSE pipeline development version 2.5.0 (Weilbacher et al. 2012, 2014) launched by the EsoRex tool. We followed the usual steps of bias subtraction, flat-fielding using lamp-flat, wavelength calibration, and twilight sky correction. We also applied the usual illumination correction using a lamp-flat exposure taken just minutes before the first science exposures. No standard star was observed on April 22, so we used data of EG 274 exposed under the same instrumental conditions in the night of April 20, 2018, to compute atmospheric throughput and characterize telluric absorption. We then created sky continuum and a first-guess sky line flux table using the offset sky exposure. The NFM is operated with an

atmospheric dispersion compensator, so no software correction was necessary. We flux-calibrated the data, subtracted the sky continuum, and rescaled the sky line fluxes to the actual exposures and subtracted them, before correcting the data for barycentric velocity (of 17.2 km s^{-1}). We finally applied the astrometric distortion correction specific to NFM, computed the relative offsets of the four exposures, and combined them into one final datacube. This cube encompasses the data of all four exposures, but due to the large offsets it has empty regions in the outer corners (see Fig. 1).

2.3. Absolute positioning

The absolute positions of the optical regions in NGC 6240 were calibrated with respect to *Gaia* data. For positioning, we shifted the pixel reference coordinates so that the coordinates of the two sources from *Gaia* DR2 (Lindegren et al. 2016) in the field overlap with peaks N and S2, as detected in the *I* band reconstructed from the MUSE data. Since the positions of the two peaks can be made to agree with the *Gaia* DR2 positions, this implies that our absolute astrometric accuracy is about 30 mas (see Sect. 3.3).

3. Results

3.1. Continuum and emission line morphology

Figure 1 shows the field of NGC 6240 in the $H\alpha$ /[NII] line complex covered by the four overlapping MUSE observations. The $H\alpha$ line traces the distribution of the ionized gas. Clearly, the emission line gas is distributed irregularly due to the merging process. Overlaid are *I*-band contour levels. The white square indicates the size of the zoomed-in area in Figs. 2, 3, 9, and 10.

The inner region of NGC 6240 is shown in Fig. 2 in the Cousins *I* band (effective central wavelength at $\lambda 8797 \text{ \AA}$). This wavelength range traces the old stellar component. The circles and ellipses are based on the three maximum intensity positions in the *I* band (N, S1, S2) where we extracted spectra. In addition, we extracted a spectrum in the region Sx located between the emission regions S1 and S2. Table 1 gives the coordinates of the *I*-band continuum peaks, of Sx, and of the MERLIN and VLBA radio sources N-G04 and S-G04 where we extracted spectra as well.

The zoomed-in region of NGC 6240 in the $H\alpha$ /[NII] line is shown in Fig. 3. The maxima of the southern peaks in the *I* band correspond to the peaks of $H\alpha$ emission. However, there is a slight offset for the northern peak. The projected distance between the optical maxima of the northern N and S1 component (*I* band) amounts to 1.81 ± 0.03 arcsec (856 ± 14 pc); the projected distance between the two southern components S1 and S2 amounts to 0.42 ± 0.03 arcsec (198 ± 14 pc).

3.2. Spatial resolution

The characterization of the point spread function (PSF) of the NFM data is still ongoing. Our field does not contain any unresolved objects and we do not know of a higher resolution image of the field, so we cannot derive a firm measurement of the FWHM of our data. However, we reconstructed an image corresponding to the HST ACS F814W filter from the MUSE data, and we can visually see smaller details than in the HST ACS data (FWHM of $0''.1$, HST proposal ID 10595, PI A. Evans) taken in that filter. We therefore assume an approximate core resolution of ~ 75 mas in the MUSE NFM data at the red end of the wavelength range. We present observations of the inner region of NGC 6240 taken with the ACS camera on board the

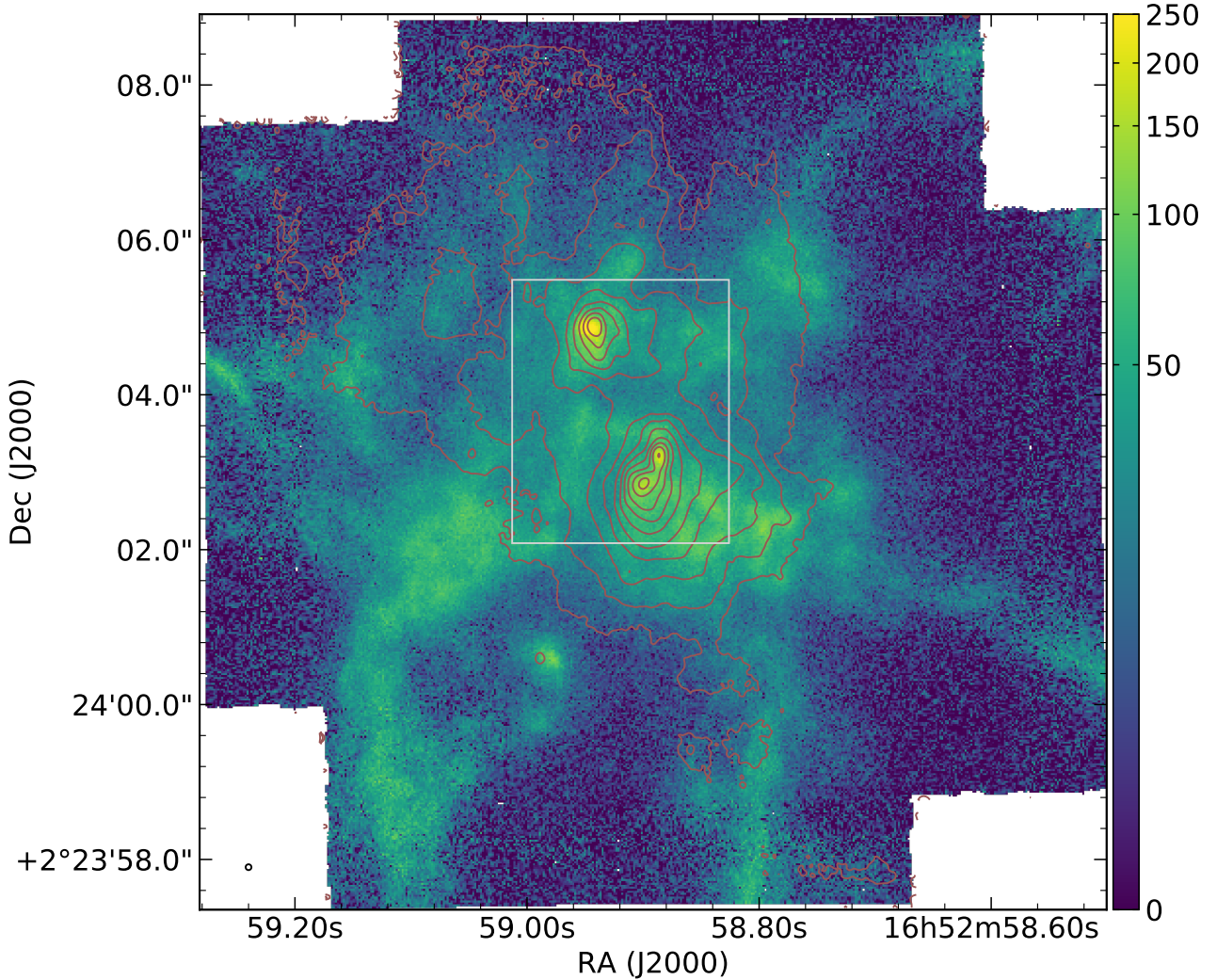


Fig. 1. $H\alpha$ /[NII] image of the gas in NGC 6240. North is to the top and east to the left. Overlaid are I band contour levels (see Fig. 2). The white square indicates the size of the zoomed-in region in Figs. 2, 3, 9, and 10. The estimated spatial resolution at FWHM of 75 mas (35 pc) is plotted in the bottom left corner of each image. The flux is given in units of 10^{-20} erg cm^{-2} s^{-1} pix^{-1} .

HST and for comparison a MUSE image in Fig. 4. At the distance of NGC 6240 we therefore cover a region of 3.5 kpc in each exposure with a spatial resolution of about 35 pc.

3.3. Absolute positional accuracy

The absolute positional accuracy of our optical positions in NGC 6240 is very high as they have been calibrated with respect to *Gaia* data. Therefore, the given positions of the emission and the absorption regions have an absolute error of only 30 mas. We show the *Gaia* positions of the regions N and S2 before and after absolute calibration of our MUSE data in Fig. 5. The optical continuum and emission line peak S1 coincides with the center of the blueshifted stellar component (Fig. 9) and with the maximum of the stellar velocity dispersion (Fig. 10), and with the southern radio component S-G04 based on the MERLIN and VLBA data (Gallimore & Beswick 2004). All these positions agree within 0.08 arcsec.

3.4. Emission line spectroscopy

We present the spectra of the emission regions N, S1, S2, and of the region Sx between S1 and S2 in Fig. 6. In addition,

we show the spectra extracted at the positions of the northern (N-G04) and southern (S-G04) MERLIN and VLBA radio positions (Gallimore & Beswick 2004). The corresponding spatial regions (ellipses) we used to extract the spectral flux of the individual regions are shown in Figs. 2 and 3. The sizes and orientations of the radio ellipses adopted are from the MERLIN observations (Gallimore & Beswick 2004). The centers of the N, S1, and S2 ellipses are based on the maxima of the I -band contour levels. The diameters of the ellipses correspond to a value of three to five times that of our spatial resolution. The Sx ellipse was chosen in order to fit between those of S1 and S2. The exact sizes of the ellipses of the individual line emitting regions are given in Table 2. All the observed spectra show a strong red continuum because of heavy dust absorption.

We determined the redshifts, the line intensities, and the line widths (FWHM) of the strongest emission lines in the individual line emitting regions (see Appendix A). We fitted the $H\alpha$ line complex by multiple Gaussians with the IRAF task SPLOT. Here we set the additional condition that both [NII] lines must hold the same width. The redshifts of the individual emission regions were fixed on the basis of the $H\alpha$ line, the strongest emission line. The Balmer lines as well as the [NII] and [OIII]5007 lines show very similar redshifts at the individual positions in NGC 6240.

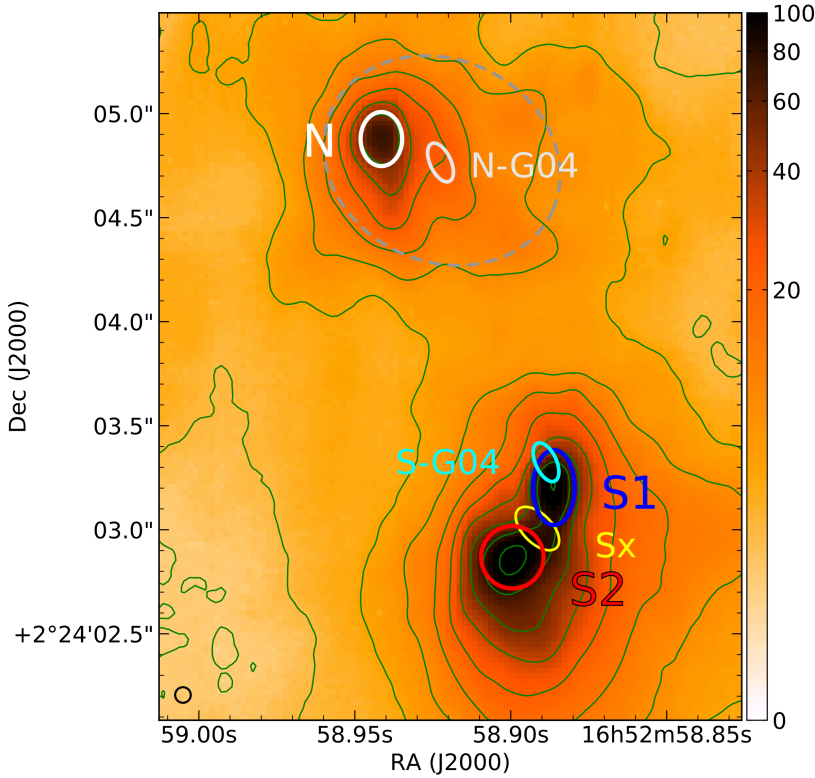


Fig. 2. Cousins I -band image (intensities and contours) of the zoomed-in region in NGC 6240. The Cousins I band mostly traces the integrated distribution of the old stellar component. Spectra were extracted at the three locations corresponding to peaks of maximum intensity in the I -band map (N, S1, S2, indicated by circles or ellipses). Also indicated are the positions of the two MERLIN and VLBA radio sources N-G04 and S-G04 (Gallimore & Beswick 2004), and the region Sx between the components S1 and S2. The size of the northern stellar bulge component, based on the near-infrared CaII triplet lines (see Sect. 3.5 and Figs. 3, 9, 10), is indicated by the dashed ellipse. The flux is given in units of 10^{-20} erg cm^{-2} s^{-1} pix^{-1} .

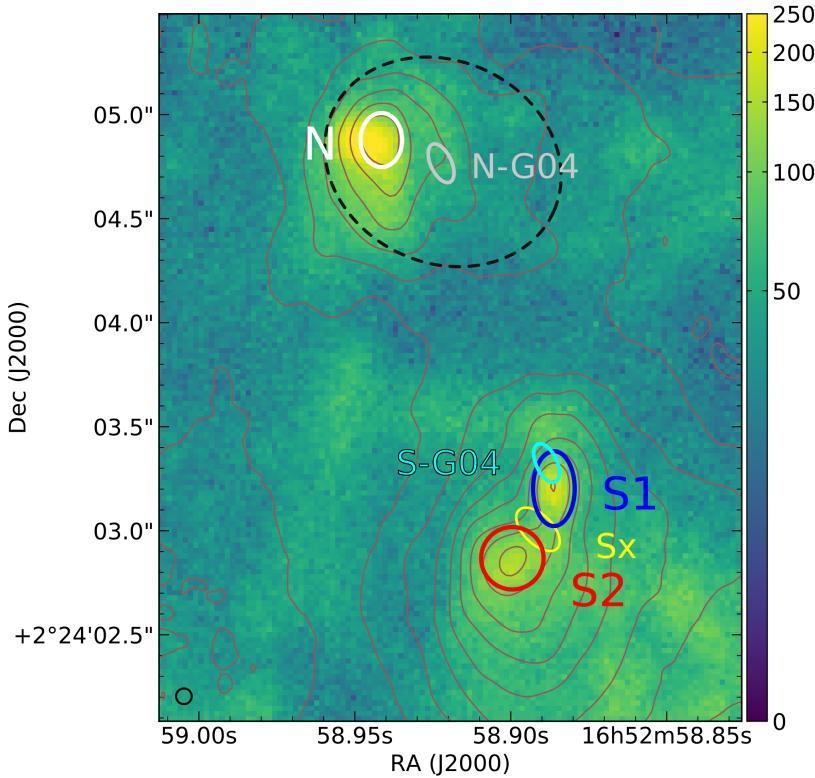


Fig. 3. $H\alpha$ /[NII] image of the zoomed-in white square in Fig. 1. Again, I -band contour levels are overlaid. Spectra were extracted at the three locations corresponding to the peaks of maximum intensity in the I -band map (N, S1, S2, indicated by circles or ellipses). Also indicated are the positions of the two MERLIN and VLBA radio sources N-G04 and S-G04 (Gallimore & Beswick 2004). The flux is given in units of 10^{-20} erg cm^{-2} s^{-1} pix^{-1} .

However, the [OI]6300 line deviates by up to 150 km s^{-1} to higher and to lower redshifts, indicating that this line originates at different layers in NGC 6240 compared to the other emission lines. The [OI]/ $H\alpha$ /[SII] complex of the components N and S1 is shown in Fig. 7. The spectra have been shifted to the same $H\alpha$ velocity and scaled to similar $H\alpha$ intensities. It can be seen that the relative velocities of the [OI] and [SII] lines do not agree with those of the $H\alpha$ and [NII] lines.

It is evident from the $H\alpha$ /[NII] and [SII] line spectra (Fig. 6) that the observed emission line profiles of the regions S2 and Sx are quite complex. More precisely, each spectrum is a superposition of at least two emission components (Figs. 6 and 8). On the other hand, the $H\alpha$ /[NII] complex of the S1 region can easily be fitted with only one emission component. To decompose the S2 and Sx spectra, we made the assumption that one of the components shows emission line profiles with

Table 1. *I*-band continuum peaks of the northern component N and the southern components S1 and S2.

ID	RA (J2000)	Dec (J2000)
N	16:52:58.943±.0005	+2:24:04.89±.003
N-G04	16:52:58.924±.0003	+2:24:04.766±.002
S-G04	16:52:58.890±.0003	+2:24:03.337±.002
S1	16:52:58.888±.0005	+2:24:03.22±.003
Sx	16:52:58.893±.0015	+2:24:03.02±.01
S2	16:52:58.901±.0015	+2:24:02.88±.01

Notes. Also listed is the position Sx where we took a spectrum between the components S1 and S2. The optical errors are 1σ errors (1D modeling). The MERLIN and VLBA radio sources N-G04 and S-G04 at 2.4 and 1.7 GHz are also given (Gallimore & Beswick 2004).

a similar spectral shape to that of the S1 complex. Thus, we subtracted a series of shifted and scaled S1 spectra from the S2 and Sx spectra until the difference spectrum resulted in an $H\alpha$ /[NII] complex where all the lines showed similar line widths and where the [NII] line ratio corresponded to the theoretical ratio of 1/3. As our best solution we subtracted a scaled (by 34%) and shifted (by 222 km s^{-1}) S1 spectrum from the $H\alpha$ /[NII] and [SII] complex in S2 (see Fig. 8) and in Sx. The resulting clean S2 spectrum is a better match for a single nucleus spectrum. From here on the spectra of S2 and Sx refer to this clean version (Tables 3, 4, A.5, A.6).

We derived the dust extinction in the individual emitting regions based on the Balmer decrement $H\alpha/H\beta$ using the formulas given by Dominguez et al. (2013). We calculated high extinction values A_V (on the order of ten) at all five component positions except at the northern region N, indicating a lower extinction of only $A_V = 5$ (see Table 3). Furthermore, the dust extinction could in principle also be estimated from the spectral energy distribution. We see some trends between the two estimates regarding the amount of dust in NGC 6240. The northern component N shows the smallest Balmer decrement and the flattest spectral continuum flux distribution, while the component S1 shows the highest Balmer decrement and a very steep continuum slope. However, it is known that the stellar continuum reddening shows no clear correlation with the dust content, suggesting that the distribution of stellar reddening does not act as a good tracer of the overall dust content (e.g., Kreckel et al. 2013).

We determined the ionization level of the individual emission regions based on optical emission-line ratios i.e., diagnostic diagrams based on the line intensity ratios of [OIII]5007/ $H\beta$ versus [NII]6584/ $H\alpha$ (Kauffmann et al. 2003; Kewley et al. 2006). The line ratios of the individual emission regions and of the radio sources are given in Table 3. The line ratios of all investigated spectra (Fig. 6) correspond to LINER-like objects. Although all spectra fall in the LINER region in the diagnostic diagram, it is unlikely that all of them are caused by photoionization from individual active nuclei (see Sect. 4.1). Furthermore, we observe emission line widths of 500 to 700 km s^{-1} (Appendix A). Such high line widths are rarely observed in LINER nuclei.

3.5. Stellar kinematics

To derive stellar kinematics around the continuum peaks, we processed the MUSE cube using pPXF v6.7.12 (Cappellari & Emsellem 2004; Cappellari 2017). Since the S/N was only sufficient in the red part to see continuum features, we restricted the wavelength range to 8350 – 9200 \AA . This wavelength range

includes the near-infrared Ca II triplet lines (8498 , 8542 , 8662 \AA). We used a set of 53 high-quality stars from the Indo-US library as stellar templates (Valdes et al. 2004; Shetty & Cappellari 2015; Guérou et al. 2017). This library provides a high enough resolution compared to the MUSE data, and fully covers the wavelength range of interest. We convolved the templates to an estimate of the average instrumental width and then used pPXF to fit velocity and velocity dispersion for every spectrum. Since the fit only converges to sensible values of continuum kinematics around the peaks, we cleaned up strongly deviant fits and those where the outputs are identical to the starting values.

Based on the presence of the near-infrared calcium II triplet lines, which are very strong in K giant stars and can be observed in high-extinction regions such as galactic bulges, we deduced the existence of old stellar bulge components in NGC 6240 (e.g., Vasquez et al. 2015 and references therein). Consequently, we used the calcium II triplet lines to derive the redshift and the stellar dispersion of the old stellar bulge components. The resulting maps are shown in Figs. 9 and 10. A strong signal of an old stellar bulge component is seen in the northern region next to the northern emission region N, and at each of the two southern emission line regions S1 and S2. We present in Table 4 the absorption line velocities and velocity dispersions based on the CaII IR triplet lines for the components N, S1, and S2, and for the positions of the MERLIN and VLBA radio sources N-G04 and S-G04 and at Sx. The region S2 shows a small gradient in the absorption velocity and in the stellar dispersion (Figs. 9 and 10). Therefore, we measured these S2 component values using a radius that is 20% smaller in order to exclude the gradient. For comparison we present the emission line velocities and the line widths (FWHM) based on the $H\alpha$ emission line for the same regions (see Table 4).

3.6. Black hole masses

We determined stellar velocity dispersions at the positions of the optical emission maxima S1 and S2 and at the radio positions (Fig. 10, Table 4). Hereafter, we assume that the components S-G04 and S1 originate from the same nucleus as their positions overlap. We identify each of the emission regions N-G04, S-G04/S1, and S2 to be separate nuclei in the centers of independent galactic bulges, hence each of these emission regions is associated with a SMBH. Based on the radio emission, this assumption is obviously justified for N-G04 and S-G04/S1. Although we are not able to resolve the sphere of influence for a black hole in S2 and do not observe an accretion signature, we find strong evidence for the existence of an independent nucleus S2 (see Sects. 4.2–4.4). We calculate corresponding black hole masses M_{BH} for each of the nuclei by using the tight correlation between the stellar velocity dispersion σ_{star} in galaxy bulges and M_{BH} in inactive and active galaxies (e.g., Gebhardt et al. 2000; Greene & Ho 2006). The observed velocity dispersion values correspond to black hole masses of

$$\begin{aligned}
M(\text{N-G04}) &= 3.6 \pm 0.8 \times 10^8 M_{\odot}, \\
M(\text{S-G04/S1}) &= 7.1 \pm 0.8 \times 10^8 M_{\odot}, \\
M(\text{S2}) &= 9.0 \pm 0.7 \times 10^7 M_{\odot}
\end{aligned}$$

when using the $M_{\text{BH}}-\sigma_{\text{star}}$ diagram of Greene & Ho (2006). The resulting black hole mass ratio of the triple system is $[4 : 8 : 1]$ for [N-G04 : S-G04/S1 : S2].

We did not derive a black hole mass for component N as it is not connected with a separate nucleus, but is located in the foreground at the edge of the northern bulge (see Sect. 4.4).

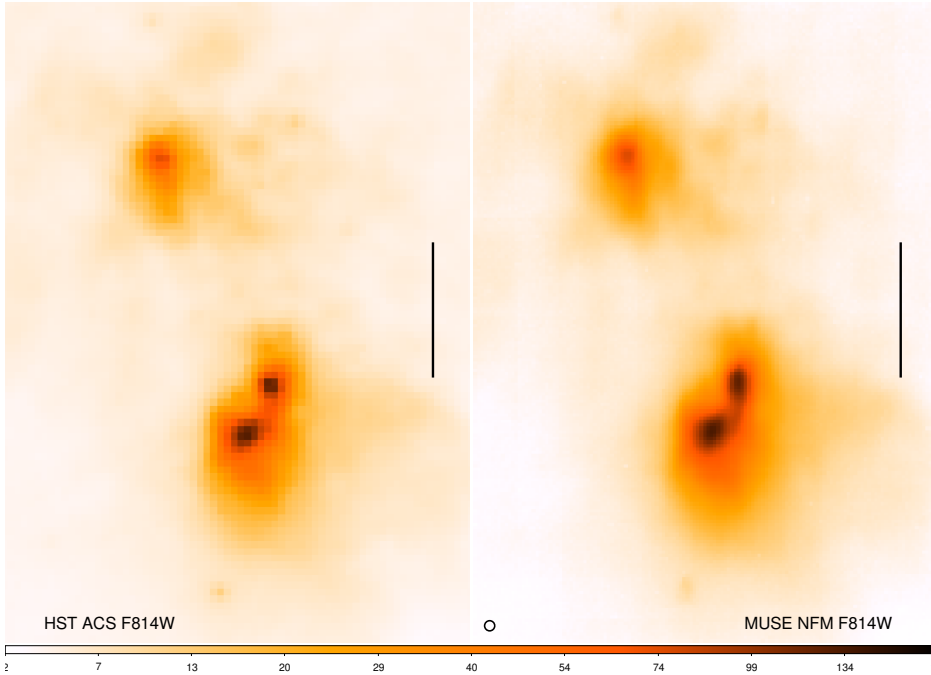


Fig. 4. Images of NGC 6240 taken with the HST-ACS and F814W filter and with MUSE in the NFM for the I -band. The black line is 1 arcsec long. An inverse asinh scaling was used for the color map.

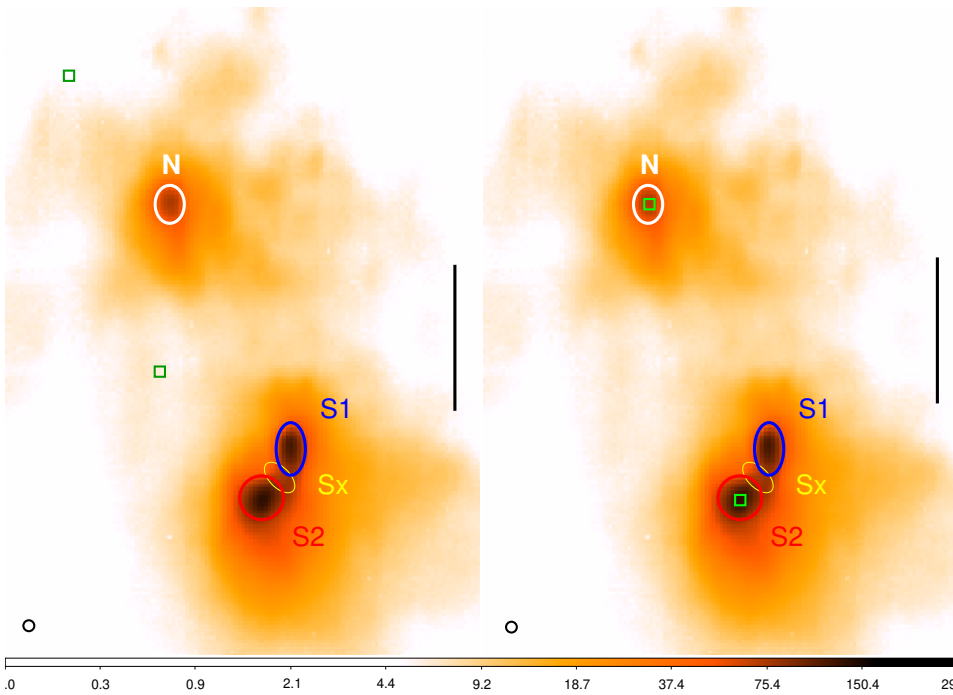


Fig. 5. Positions of *Gaia* sources (green squares) and MUSE sources before (*left*) and after (*right*) absolute calibration of the MUSE data. The black line is 1 arcsec long. An inverse log scaling was used for the color map.

Deriving the orbital mass M_{orb} (Petrosyan 1983) offers another way to estimate the integrated mass of a double nucleus system. Making the assumption that both nuclei S1 and S2 are in circular motion about a common center and knowing the radial velocity difference between the nuclei (270 km s^{-1}) and their projected distance (198 pc), we calculated the orbital mass M_{orb} of the S1–S2 system using the equation (Petrosyan 1983)

$$M_{\text{orb}} = \frac{32}{3\pi} (\Delta V)_{\text{pr}}^2 \frac{D_{\text{pr}}}{G}, \quad (1)$$

where $\frac{32}{3\pi}$ is a mean projection factor. We derive an orbital mass M_{orb} of $1.2 \times 10^{10} M_{\odot}$. Since the orbital mass is usually higher than the mass of the two individual nuclei, this result fits with

the black hole masses derived on the basis of the stellar velocity dispersion.

4. Discussion

4.1. Excitation of the emission lines in the central region of NGC 6240

NGC 6240 is classified as a LINER type in a previous work (Veilleux et al. 1995) based on an integrated optical spectrum of the central region. Instead, we determined the activity level of all the individual central emission regions based on their optical emission-line ratios (Table 3). The line ratios of all six investigated spectra (Fig. 6) correspond to LINER-like objects. Figure 11 shows the $[\text{OIII}]5007/\text{H}\beta$ versus $[\text{NII}]6584/\text{H}\alpha$ line

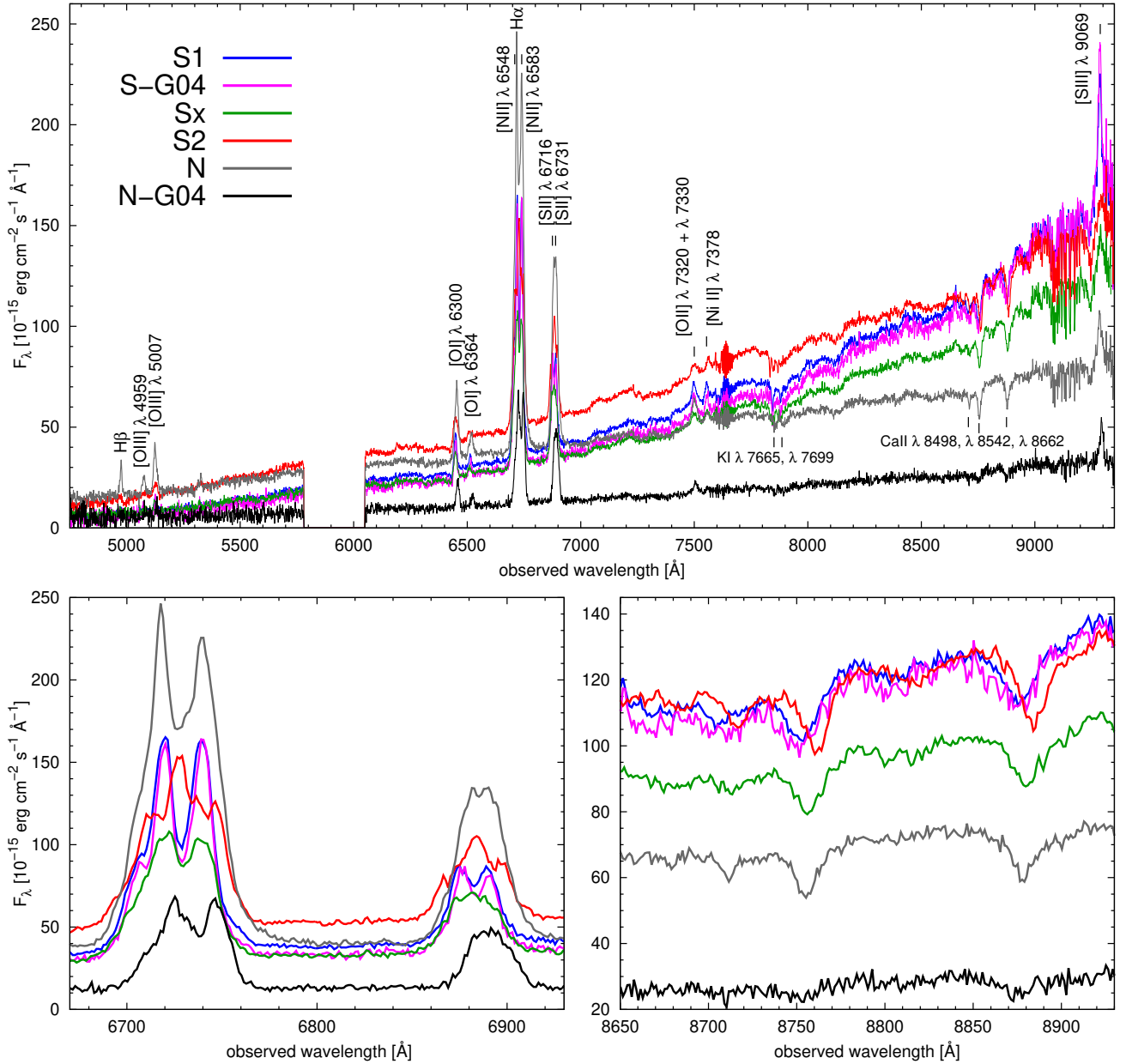


Fig. 6. Spectra of the northern N (gray) and southern S1 (blue) and S2 (red) emission regions, of the northern N-G04 (black) and southern S-G04 (pink) MERLIN and VLBA radio positions, and the region Sx between the southern components. In the *lower panels* are shown enlargements of the H α /[SII] complex and of the near-infrared CaII triplet lines.

Table 2. Sizes of the ellipses of the individual line emitting regions.

Component	Minor axis [arcsec]	Major axis [arcsec]	Angle [deg]
N	0.10	0.13	0
N-G04	0.05	0.10	25
S-G04	0.05	0.10	25
S1	0.10	0.18	0
Sx	0.07	0.13	45
S2	0.15	0.15	0

diagnostic diagram for the individual emission regions. However, all the observed line ratios are consistent with shock heating models as well (see the models of Allen et al. 2008).

It is unlikely that all the individual spectra in NGC 6240 are caused by photoionization from six individual active nuclei. Alternatively, the observed line ratios can instead be explained by shock heating (e.g., Dopita & Sutherland 2013; Monreal-Ibero et al. 2010; Marziani et al. 2017). Narrow emission line widths (FWHM) of 500 to 700 km s⁻¹, like those seen in NGC 6240, are rarely observed in Seyfert and LINER nuclei (e.g., Ho et al. 2003; Zhang et al. 2013). The nuclei S1 and S2 exhibit line widths of 600 km s⁻¹; the Balmer lines of the northern regions indicate emission line widths of the same order.

In the northern region N the line widths of the nitrogen and oxygen lines are even broader (by 400 km s⁻¹) in comparison to H α (see Table A.2). These observed line profiles might be a superposition of many components originating in different regions. Emission lines broader than 600 km s⁻¹ are known from radio galaxies and luminous infrared galaxies (LIRGs), due to

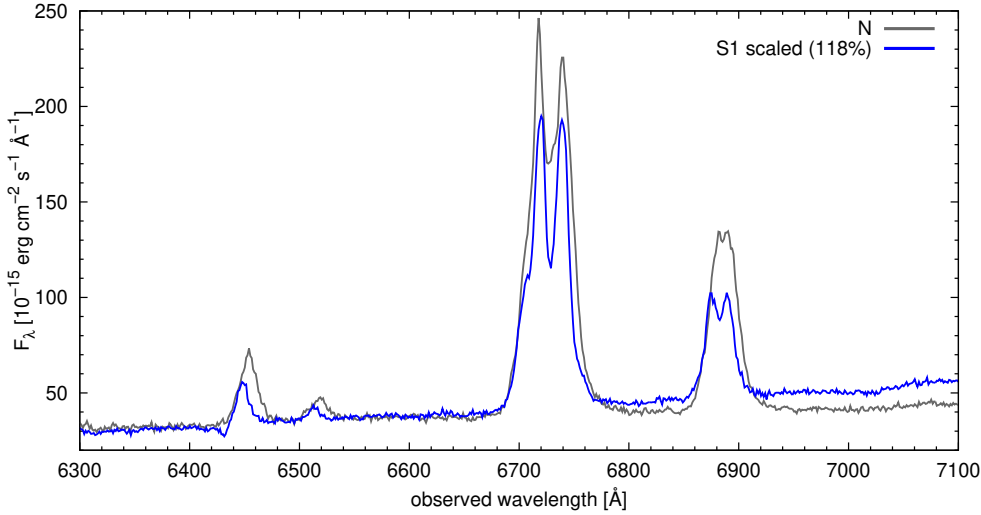


Fig. 7. Spectra of the emission regions N (gray) and S1 (blue) scaled to the same $H\alpha$ velocity.

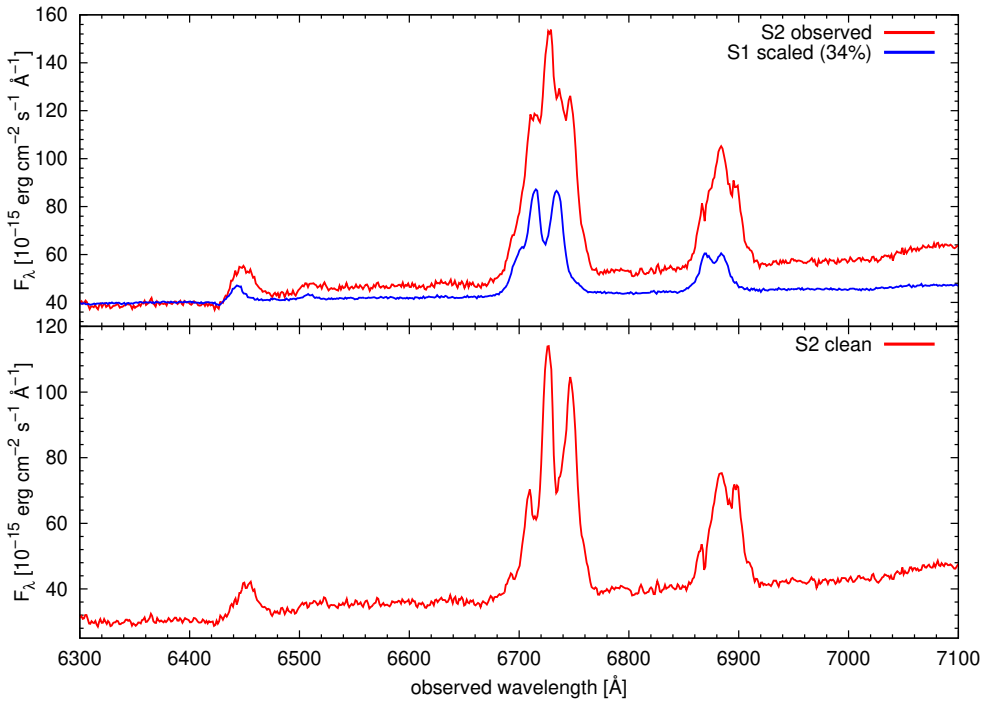


Fig. 8. Raw spectrum of S2 (red) and a scaled (by 34%) S1 spectrum shifted by 222 km s^{-1} (blue). The difference spectrum at the *bottom* shows the clean S2 spectrum.

Table 3. Balmer decrement and line intensity ratios of $[\text{N II}] \lambda 6584/H\alpha$ and $[\text{O III}] \lambda 5007/H\beta$ (BPT diagram) for the components N, S1, S2, Sx, and for the spectra taken at the radio positions.

Intensity ratio	N	N-G04	S-G04	S1	Sx	S2
$H\alpha/H\beta$	12.1	54.:	73.:	64.	27.	45.:
A_V	5.0	10.2:	11.2:	10.8	7.8	9.5:
$\log([\text{NII}]/H\alpha)$	0.327 ± 0.018	0.064 ± 0.018	0.055 ± 0.018	0.047 ± 0.019	0.031 ± 0.020	0.068 ± 0.019
$\log([\text{OIII}]/H\beta)$	0.371 ± 0.025	0.710 ± 0.146	0.577 ± 0.071	0.507 ± 0.025	0.403 ± 0.220	0.434 ± 0.066

additional motions caused by radio jets and/or galaxy merging processes including outflowing processes (e.g., [Buchanan et al. 2006](#)). It is therefore intriguing that a small-scale radio jet has been detected at the position of N-G04 ([Gallimore & Beswick 2004](#); [Hagiwara et al. 2011](#)). NGC 6240 is both a merger and an LIRG and as such displays broad line widths caused by a superposition of different components including turbulent motions.

Radio supernova and narrow H_2O maser lines near the S-G04 region suggest some circumnuclear star formation and dense molecular gas ([Hagiwara et al. 2011](#)). Hence, all observed emission line spectra in NGC 6240 are almost certainly caused by shock heating. An independent confirmation of shock heated gas comes from spatially resolved hard X-ray emission in the central 5 kpc detected on deep *Chandra* images ([Wang et al. 2014](#)).

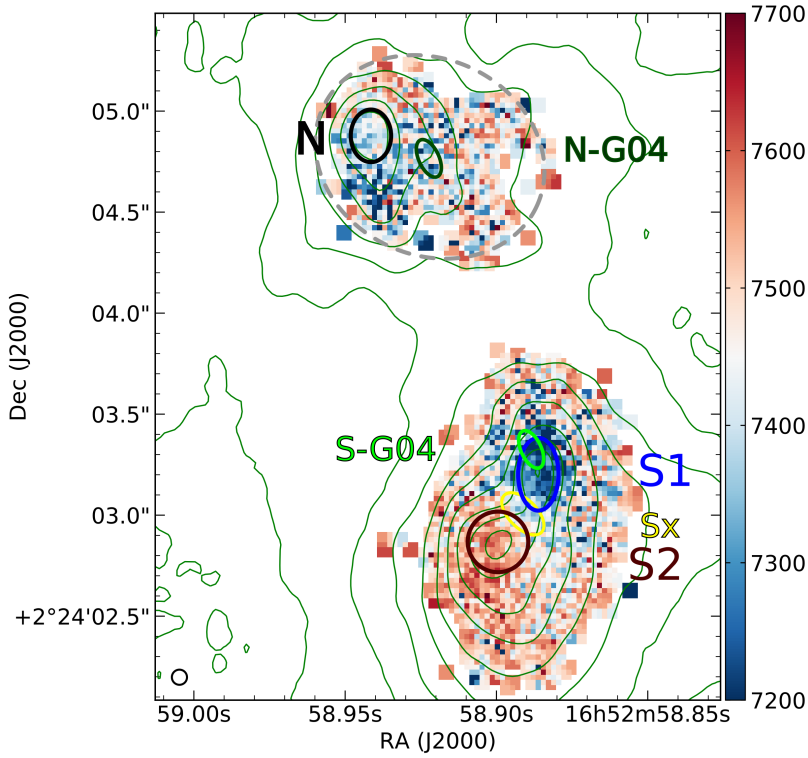


Fig. 9. Redshift of the stellar component based on the CaII IR triplet lines in units of km s^{-1} for the northern and southern nuclear bulge regions. White regions represent locations where the S/N was not high enough to obtain good fits. The size of the northern stellar bulge component is indicated by the dashed ellipse (see also Fig. 10).

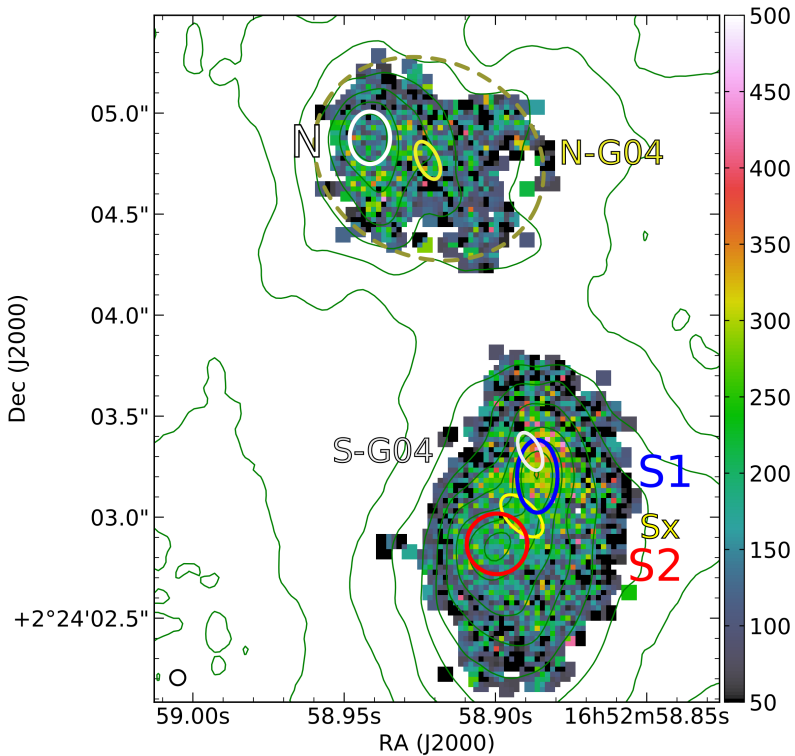


Fig. 10. Stellar dispersion map of the northern and southern nuclear bulge regions based on the CaII IR triplet lines in units of km s^{-1} . White regions represent locations where the S/N was not high enough to obtain good fits.

4.2. Black hole masses

We derived the stellar velocity dispersions at the northern and southern radio sources and at S2. Afterwards we determined black hole masses of $M(\text{N-G04}) = 3.6 \pm 0.8 \times 10^8 M_\odot$, $M(\text{S-G04/S1}) = 7.1 \pm 0.8 \times 10^8 M_\odot$, and $M(\text{S2}) = 9.0 \pm 0.7 \times 10^7 M_\odot$ based on the $M_{\text{BH}}-\sigma_{\text{star}}$ diagram of Greene & Ho (2006). Furthermore, we calculated the orbital mass M_{orb} of the S1–S2 system (using Eq. (1)) to be $M_{\text{orb}} = 1.2 \times 10^{10} M_\odot$. Assuming

a relaxed gravitationally bound S1–S2 system, and considering an S2 radius of $\sim 100 \text{ pc}$ and velocity dispersion of 180 km s^{-1} , an isothermal sphere would have a mass of $\sim 7 \times 10^8 M_\odot$. The size of S2 is therefore comparable to that of Omega Centauri, but ~ 200 times more massive; S2 is therefore unlikely to be a huge globular cluster given the predictions of some current models (Schulz et al. 2015). It does mean, however, that the BH mass (as estimated by the Greene & Ho formalism) is 13% of the mass of the S2 region, which is significantly above the standard M_{BH}

Table 4. Absorption line velocities and velocity dispersions based on the CaII IR triplet lines for the components N, S1, and S2, and on the positions of the MERLIN and VLBA radio sources N-G04 and S-G04.

Component	v (CaII) [km s ⁻¹]	σ (CaII) [km s ⁻¹]	v (H α) [km s ⁻¹]	$FWHM$ (H α) [km s ⁻¹]	σ (H α) [km s ⁻¹]
N	7404. \pm 13.	157. \pm 13.	7117.4 \pm 5.	602. \pm 16.	256. \pm 8.
N-G04	7297. \pm 41.	282. \pm 31.	7473.9 \pm 5.	677. \pm 20.	288. \pm 9.
S-G04	7202. \pm 21.	316. \pm 35.	7176.8 \pm 9.	578. \pm 17.	246. \pm 8.
S1	7260. \pm 29.	297. \pm 29.	7163.1 \pm 5.	605. \pm 22.	257. \pm 10.
Sx	7422. \pm 20.	203. \pm 28.	7528.8 \pm 9.	553. \pm 22.	235. \pm 10.
S2	7530. \pm 15.	180. \pm 30.	7473.9 \pm 9.	508. \pm 15.	216. \pm 8.

Notes. For comparison we present the emission line velocities and the line widths (FWHM and σ) based on the H α line.

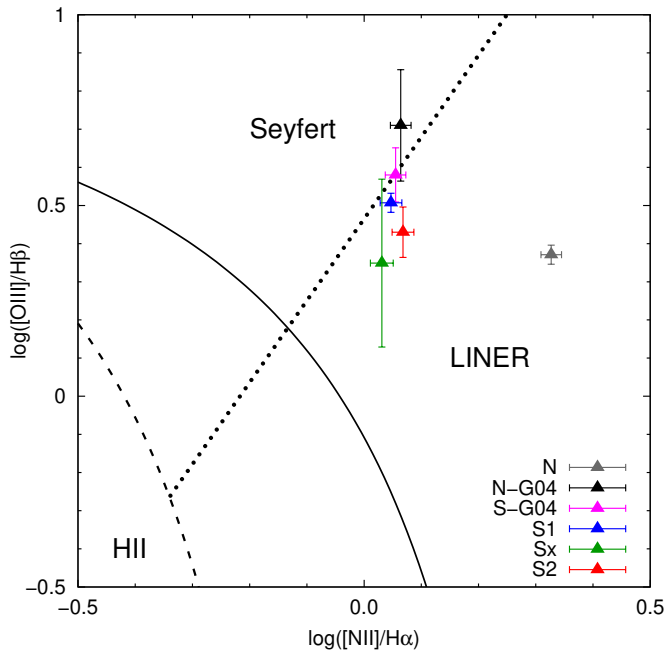


Fig. 11. Diagnostic BPT diagram of [OIII]5007/H β vs. [NII]6584/H α for individual emission line regions in NGC 6240. The dashed lines and solid lines are the dividing lines between AGN (upper right) and HII-region galaxies (lower left) (Kauffmann et al. 2003; Kewley et al. 2006). The dotted line is the dividing line between Seyfert and LINER nuclei.

to-bulge mass ratio (Haering & Rix 2004), implying significant tidal stripping of the S2 mass – and that of S1 and N-G04 – during merging. S1 and N-G04 host black holes with masses that are four to eight times higher than that of S2. Stellar velocity dispersions are systematically higher in mergers than in isolated AGN host galaxies (e.g., Liu et al. 2012; Stickley & Canalizo 2014; Medling et al. 2015). Therefore, the black hole masses, based on the velocity dispersion, might be overestimated.

The masses we determined for the black holes in the nuclei N-G04, S-G04/S1, and S2 are on the same order as those previously reported by other authors. Based on SINFONI data Engel et al. (2010) determine dynamical masses (Jeans modeling within $r < 250$ pc each) of the northern (N) and combined southern (S1+S2) nuclei based on the CO absorption bandhead: $2.5 \times 10^9 M_{\odot}$ (N) and $1.3 \times 10^{10} M_{\odot}$ (S1+S2). Based on the stellar dispersion $\sigma_{\text{star}} = 200 \text{ km s}^{-1}$ (N) and 220 km s^{-1} (S) and using the $M_{\text{BH}}-\sigma_{\text{star}}$ relation of Tremaine et al. (2002), they estimate black hole masses of $1.4 \pm 0.4 \times 10^8 M_{\odot}$ (N) and $2.0 \pm 0.4 \times 10^8 M_{\odot}$ (S1+S2). Medling et al. (2011) derive a mass of the combined southern system (S1+S2) based on Keck II Laser guide star adaptive optics using OSIRIS data of the K -band CO absorption

bandheads to trace stellar kinematics and Jeans modeling. They determine an upper limit of $2.0 \pm 0.2 \times 10^9 M_{\odot}$ and a lower limit of $8.7 \pm 0.3 \times 10^8 M_{\odot}$. However, their absolute positioning of the black hole between the nuclei S1 and S2 (their Figs. 5 and 6) is inconsistent as the southern MERLIN and VLBA radio source is overlaid on the S1 nucleus (see Figs. 9 and 10).

We did not derive an orbital mass for the N-G04 and S1–S2 system as the velocity difference between N-G04 and the S1–S2 system is quite small. A statistical formula like that of Petrosyan (1983) would lead to large errors in the mass determination.

4.3. Merging history of the southern nuclei

A schematic view of the general collision geometry in NGC 6240 is presented in Tecza et al. (2000). They assume that the southern (double) nucleus is moving in the northeastern direction (their Fig. 11). This is in accordance with the I -band contour levels, caused by the old stellar component, that are denser towards the northeastern direction than the western direction (see Figs. 1, 2). Furthermore, this concept is supported by the complex extra H α /[NII] emission component southwest of the southern double nucleus (see Fig. 12). The geometry of this extra H α emission component is reminiscent of the Magellanic stream (e.g., Nidever et al. 2008), which is composed of two filaments. The two Magellanic stream filaments show periodic and undulating spatial patterns and it is speculated that they are an imprint of the LMC rotation curve. A similar picture has evolved for the symbiotic binary system R Aqr, where H α emission is arranged in an elongated zig-zag pattern (Schmid et al. 2017). In our case the geometry of the H α filaments might be caused by the orbit of the S1 and S2 components around each other in combination with the general propagation of the southern double nucleus in the northeastern direction. The rotational timescale of S1 and S2 around each other (1 orbit) amounts to $\sim 4 \times 10^6$ years, based on the rotational velocity ($v = 158 \text{ km s}^{-1}$) of the nuclei and on the S1 and S2 distance (198 pc). We see about two and a half loops in Fig. 12 corresponding to 1.25 orbits per nucleus under the simplified assumption of circular motion. The same loop structure is seen not only in H α , but also in the emission lines of [OI], [NII], and [SII] (see the [SII] structure in the Appendix (Fig. A.1)). Based on these loops we derive a look-back time of the past motion of the S1 and S2 nuclei from the southwest on the order of 5×10^6 years. A more detailed simulation is beyond the scope of this manuscript.

4.4. Triple nucleus system in NGC 6240

The superposition of the optical images with the radio maps of Gallimore & Beswick (2004) shows that the northern active nucleus N-G04 is centrally located in the northern bulge region,

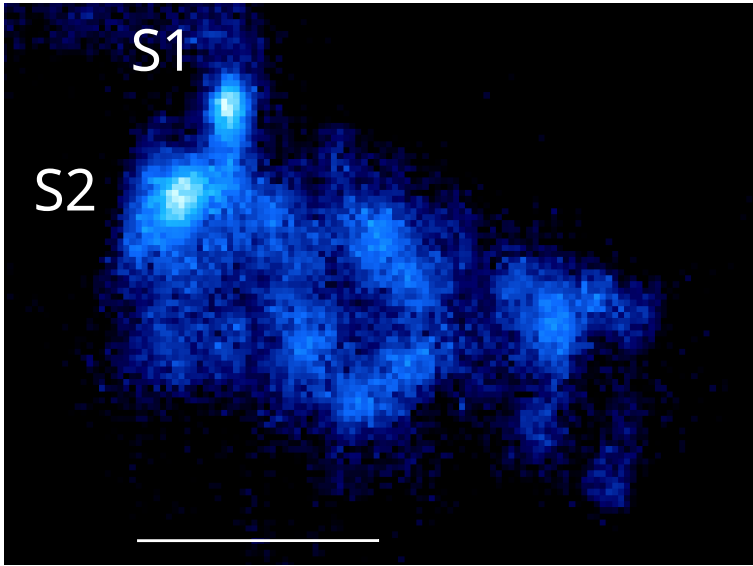


Fig. 12. Enlarged $H\alpha/[NII]$ image of the nuclei S1 and S2 and of the region southwest of the nuclei. North is to the top and east to the left. The white line is 1 arcsec long.

based on the CaII IR strength of late-type giants. This position is neither identical with the northern optical emission N at a distance of 0.33 arcsec nor with the IR emission “North 2” mentioned by [Max et al. \(2005\)](#). The northern optical emission N is located at the edge of the bulge region (see Figs. 9, 10). This emission of the N region might originate in the foreground as it shows the lowest absorption.

We propose that the southern components S1 and S2, formerly thought to be one nucleus, are in fact two distinct nuclei. Specifically, S1 and S2 are two distinct entities in terms of

- i. ionized gas structure (Fig. 1);
- ii. stellar structure (Fig. 2);
- iii. spectral features in absorption and emission (Fig. 6);
- iv. their merging history (Fig. 12).

More precisely, the $H\alpha$ redshifts of the gaseous components of S1 and S2 are comparable to the CaII IR absorption line redshifts of S1 and S2 (Table 4).

The absorption components associated with the nuclei arise in two distinct progenitor stellar bulges. These two central bulge regions S1 and S2 exhibit distinct velocity dispersions. Such a strong asymmetry in the dispersion of a stellar component orbiting only one common single nucleus would be dispersed within an orbiting timescale ([Engel et al. 2010](#)). In addition, the intensity of the continuum and of the emission lines in the intermediate region Sx is lower than that of S1 and S2. Furthermore, the intrinsic absorption in Sx is lower in comparison to the outer regions, and the recession velocity of the emission line gas in Sx is higher than in both nuclei S1 and S2. Hence, we conclude that the two southern sources S1 and S2 are two discrete nuclei separated by 198 pc that rotate around each other.

5. Conclusions

We report the discovery of three nuclei in an advanced or final state of merging within a region of only 1 kpc in NGC 6240. Thanks to MUSE we are able to show that the formerly unresolved southern component actually consists of two nuclei separated by only 198 pc. The verification and detailed study of a system with three nuclei, two of which are active and each with a mass in excess of $9 \times 10^7 M_{\odot}$, is of great importance for the understanding of hierarchical galaxy formation via merging processes ([Springel et al. 2005](#)) since multiple mergers lead to a faster evolution of massive galaxies in comparison to binary mergers. So

far it has been suggested that the formation of galactic nuclei with multiple SMBHs is expected to be rare in the local universe ([Kulkarni & Loeb 2012](#)).

The superposition of the optical images of NGC 6240 with radio maps ([Gallimore & Beswick 2004](#)) shows that the northern active nucleus N-G04 is centrally located in the northern bulge region. The southern nucleus S1 is active, based on its spatial matching with the compact radio source S-G04 ([Gallimore & Beswick 2004](#)) and its associated hard X-ray emission. However, no radio counterpart has been detected to date for the second southern nucleus S2, suggesting that it is an inactive nucleus. Overall, the inner region of NGC 6240 contains three nuclei in the final state of merging. Two of them are active with respect to their radio emission. Triple massive black hole systems might be of fundamental importance for the coalescence of massive black hole binaries in less than a Hubble time leading to the loudest sources of gravitational waves in the millihertz regime ([Bonetti et al. 2018](#) and references therein).

Acknowledgements. This work has been supported by the DFG grant Ko 857/33-1. PMW was supported by BMBF Verbundforschung (project MUSE-NFM, grant 05A17BAA). AMI acknowledges support from the Spanish MINECO through project AYA2015-68217-P. TC acknowledges support of the Agence Nationale de la Recherche (ANR) grant FOGHAR (ANR-13-BS05-0010), the OCEVU Labex (ANR-11-LABX-0060), and the A’MIDEX project (ANR-11-IDEX-0001-02) funded by the “Investissements d’avenir” French government program.

References

- Allen, M. G., Groves, B. A., Dopita, M. A., et al. 2008, *ApJS*, **178**, 20
 Bacon, R., Accardo, M., Adjali, L., et al. 2010, in *Photo-Optical Instrumentation Engineers Conference Series*, SPIE Conf. Ser., 7735, 8
 Bacon, R., Vernet, J., Borosiva, E., et al. 2014, *The Messenger*, **157**, 21
 Begelman, M. C., Blandford, R. D., & Rees, M. J. 1980, *Nature*, **287**, 307
 Bonetti, M., Haardt, F., Sesana, A., et al. 2018, *MNRAS*, **477**, 3910
 Buchanan, C. L., McGregor, P. J., Bicknell, G. V., et al. 2006, *AJ*, **132**, 27
 Cappellari, M. 2017, *MNRAS*, **466**, 798C
 Cappellari, M., & Emsellem, E. 2004, *PASP*, **116**, 138
 Dominguez, A., Siana, B., Henry, A. L., et al. 2013, *ApJ*, **763**, 145
 Dopita, M. A., & Sutherland, R. S. 2013, *ApJ*, **455**, 468
 Downes, D., Solomon, P. M., & Radford, S. J. E. 1993, *ApJ*, **414**, L13
 Engel, H., Davies, R. I., Genzel, R., et al. 2010, *A&A*, **524**, A56
 Fosbury, R. A., & Wall, J. V. 1979, *MNRAS*, **189**, 79
 Gallimore, J. F., & Beswick, R. 2004, *AJ*, **127**, 239
 Gebhardt, K., Bender, R., Bower, G., et al. 2000, *ApJ*, **539**, L13
 Genzel, R., & Cesarsky, C. J. 2000, *ARA&A*, **38**, 761

- Genzel, R., Tacconi, L. J., Rigopoulou, D., et al. 2001, *ApJ*, 563, 527
- Goulding, A. D., Pardo, K., Greene, J. E., et al. 2019, *ApJ*, 879, L21
- Greene, J. E., & Ho, L. C. 2006, *ApJ*, 641, L21
- Gu erou, A., Krajinovic, D., Epinat, B., et al. 2017, *A&A*, 608, A5
- Haering, N., & Rix, H.-W. 2004, *ApJ*, 604, L89
- Hagiwara, Y., Baan, W. A., & Kloeckner, H.-R. 2011, *AJ*, 142, 17
- Ho, L. C., Filippenko, A. V., & Sargent, W. L. W. 2003, *ApJ*, 583, 159
- Hoffman, L., & Loeb, A. 2007, *MNRAS*, 377, 957
- Kauffmann, G., Heckman, T. M., Tremonti, C., et al. 2003, *MNRAS*, 346, 1055
- Kewley, L. J., Groves, B., Kauffmann, G., et al. 2006, *MNRAS*, 372, 961
- Kollatschny, W., & Fricke, K. 1984, *A&A*, 135, 171
- Kollatschny, W., & Kowatsch, P. 1998, *A&A*, 336, L21
- Komossa, S., Burwitz, V., Hasinger, G., et al. 2003, *ApJ*, 582, L15
- Kormendy, J., & Ho, L. 2013, *ARA&A*, 51, 511
- Koss, M. J., Blecha, L., Bernhard, P., et al. 2018, *Nature*, 563, 214
- Kreckel, K., Groves, B., Schinnerer, E., et al. 2013, *ApJ*, 771, 62
- Kulkarni, G., & Loeb, A. 2012, *MNRAS*, 422, 1306
- Lindgren, L., Lammers, U., Bastrian, U., et al. 2016, *A&A*, 595, A4
- Liu, X., Shen, Y., & Strauss, M. A. 2012, *ApJ*, 745, 94
- Marziani, P., D'Onofrio, M. D., Bettoni, D., et al. 2017, *A&A*, 599, A83
- Max, C. E., Canalizo, G., Macintosh, B. A., et al. 2005, *ApJ*, 621, 738
- Max, C. E., Canalizo, G., & de Vries, W. H. 2007, *Science*, 316, 1877
- Mazzarella, J. M., Iwasawa, K., Vavilkin, T., et al. 2012, *AJ*, 144, 125
- Medling, A. M., Ammons, S. M., Max, C. E., et al. 2011, *ApJ*, 743, 32
- Medling, A. M., Vivian, U., Max, C. E., et al. 2015, *ApJ*, 803, 61
- Monreal-Ibero, A., Arribas, S., Colina, L., et al. 2010, *A&A*, 517, A28
- Netzer, H., Kollatschny, W., & Fricke, K. 1987, *A&A*, 171, 41
- Nidever, D. L., Majewski, S. R., & Butler Burton, W. 2008, *ApJ*, 679, 432
- Petrosyan, A. R. 1983, *Sov. Astron. Lett.*, 9, 179
- Satyapal, S., Secrest, N. J., Ricci, C., et al. 2017, *ApJ*, 848, 126
- Schmid, H. M., Bazzon, A., Milli, J., et al. 2017, *A&A*, 602, A53
- Schulz, C., Pflamm-Altenburg, J., & Kroupa, P. 2015, *A&A*, 582, A93
- Shetty, S., & Cappellari, M. 2015, *MNRAS*, 454, 1332
- Springel, V., White, S. D. M., Jenkins, A., et al. 2005, *Nature*, 435, 629
- Stickley, N. R., & Canalizo, G. 2014, *ApJ*, 786, 12
- Tecza, M., Genzel, R., Tacconi, L. J., et al. 2000, *ApJ*, 537, 178
- Tremaine, S., Gebhardt, K., Bender, R., et al. 2002, *ApJ*, 574, 740
- Valdes, F., Gupta, R., Rose, J. A., et al. 2004, *ApJS*, 152, 251V
- Vasquez, S., Zoccali, M., Hill, V., et al. 2015, *A&A*, 580, A121
- Veilleux, S., Kim, S.-C., & Sanders, D. B. 1995, *ApJS*, 98, 171
- Wang, J., Nardini, E., & Fabbiano, G. 2014, *ApJ*, 781, 55
- Weilbacher, P., Streicher, O., Urrutia, T., et al. 2012, in *Photo-Optical Instrumentation Engineers Conference Series*, SPIE Conf. Ser., 8451
- Weilbacher, P., Streicher, O., Urrutia, T., et al. 2014, *ASP Conf. Ser.*, 485, 451
- Wright, E. L. 2006, *PASP*, 118, 1711
- Wright, G. S., Joseph, R. D., & Meikle, W. P. S. 1984, *Nature*, 309, 430
- Zhang, Z. T., Liang, Y. C., & Hammer, F. 2013, *MNRAS*, 430, 2605

Appendix A: Information

Table A.1. N component.

Line	λ_{center} [Å]	z	v [km s ⁻¹]	F	$FWHM$ [Å]	$FWHM$ [km s ⁻¹]
[N II] λ 6583	6739.8±0.2	0.02376±0.00003	7126.5±9.	4271.±185.	22.46±0.74	1000.±33.
H α λ 6563	6718.5±0.1	0.02372±0.00002	7117.4±5.	2012.±60.	13.48±0.35	602.±16.
[N II] λ 6548	6707.3±0.5	0.02432±0.00008	7297.0±23.	1633.±57.	22.46±0.60	1005.±25.
[O I] λ 6300	6453.6 ±0.2	0.02433±0.00003	7299.5±10.	699.±28.	19.14±0.77	890.±36.
[O III] λ 5007	5126.1±0.2	0.02382±0.00004	7145.8±12.	390.±16.	16.96±0.68	992.±38.
H β λ 4861	4975.0±0.3	0.02338±0.00004	7014.0±18.	166.±8.	10.06±0.40	606.±24.

Notes. The table lists: emission line centers, redshifts, line flux F in units of 10^{-15} erg s⁻¹ cm⁻², and line widths (FWHM) of the strongest emission lines.

Table A.2. N-G04 component.

Line	λ_{center} [Å]	z	v [km s ⁻¹]	F	$FWHM$ [Å]	$FWHM$ [km s ⁻¹]
[N II] λ 6583	6746.9±0.2	0.02483±0.00003	7450.0±9.	933.3±37.	16.96±0.80	754.±30.
H α λ 6563	6726.3±0.1	0.02491±0.00002	7473.9±5.	806.2±24.	15.18±0.46	677.±20.
[N II] λ 6548	6711.4±0.5	0.02495±0.00007	7484.8±23.	360.3±14.	16.96±0.68	758.±30.
[O I] λ 6300	6458.3 ±0.2	0.02508±0.00003	7523.5±9.	239.8±11.	16.51±0.83	767.±38.
[O III] λ 5007	5132.4±0.2	0.02508±0.00004	7523.3±12.	77.0±14.	10.65±0.53	623.±31.
H β λ 4861	4981.1:±1.0	0.02464±0.00018	7390.6±60.	15.:±10.	6.:±5.	361.:±301.

Notes. The table lists: emission line centers, redshifts, line flux F in units of 10^{-15} erg s⁻¹ cm⁻², and line widths (FWHM) of the strongest emission lines.

Table A.3. S-G04 component.

Line	λ_{center} [Å]	z	v [km s ⁻¹]	F	$FWHM$ [Å]	$FWHM$ [km s ⁻¹]
[N II] λ 6583	6739.8±0.2	0.02376±0.00003	7126.5±9.	1927.±67.	13.93±0.49	620.0±22.
H α λ 6563	6719.8±0.1	0.02392±0.00002	7176.8±5.	1699.±51.	12.94±0.42	577.7±17.
[N II] λ 6548	6704.8±0.4	0.02390±0.00010	7169.8±31.	739.4±26.	13.93±0.49	623.3±22.
[O I] λ 6300	6449.1 ±0.3	0.02362±0.00004	7085.2±14.	300.2±12.	14.36±0.57	668.0±27.
[O III] λ 5007	5126.0±0.5	0.02380±0.00010	7139.8±30.	88.0 ±5.	9.81±0.44	574.1±26.
H β λ 4861	4979.0:±1.0	0.02420±0.00021	7261.0±62.	23.3: ±5.	8.45:±1.8	509.:±107.

Notes. The table lists: emission line centers, redshifts, line flux F in units of 10^{-15} erg s⁻¹ cm⁻², and line widths (FWHM) of the strongest emission lines.

Table A.4. S1 component.

Line	λ_{center} [Å]	z	v [km s ⁻¹]	F	$FWHM$ [Å]	$FWHM$ [km s ⁻¹]
[N II] λ 6583	6739.3±0.2	0.02368±0.00003	7103.8±9.	2003.±78.	14.6±0.57	650.±25.
H α λ 6563	6719.5±0.1	0.02388±0.00002	7163.1±9.	1797.±56.	13.56±0.57	605.±25.
[N II] λ 6548	6703.8±0.4	0.02379±0.00010	7137.0±31.	743.3±35.	14.6±0.57	653.±25.
[O I] λ 6300	6448.1 ±0.3	0.02346±0.00004	7037.6±14.	266.5±11.	13.5±0.54	626.±25.
[O III] λ 5007	5125.7±0.5	0.02374±0.00010	7121.9±30.	90.±5.	10.9±0.45	639.±26.
H β λ 4861	4974.3±1.0	0.02324±0.00021	6971.0±62.	28.±3.	8.42±1.0	508.±60.

Notes. The table lists: emission line centers, redshifts, line flux F in units of 10^{-15} erg s⁻¹ cm⁻², and line widths (FWHM) of the strongest emission lines.

Table A.5. Sx-clean component.

Line	λ_{center} [Å]	z	v [km s ⁻¹]	F	$FWHM$ [Å]	$FWHM$ [km s ⁻¹]
[N II] λ 6583	6748.1±0.3	0.02511±0.00005	7504.8±14.	730.9±29.	13.36±0.53	594.±24.
H α λ 6563	6727.5±0.2	0.02510±0.00003	7528.8±9.	679.8±27.	12.40±0.50	553.±22.
[N II] λ 6548	6710.5±0.5	0.02481±0.00007	7443.6±23.	220.7±9.	13.36±0.53	597.±24.
[O I] λ 6300	6455.5 ±0.5	0.02463±0.00008	7389.9±24.	124.6±6.	12.85±0.71	598.±30.
[O III] λ 5007	5131.2±1.0	0.02484±0.00019	7451.4±60.	63.5±16.	15.68:±4.	916.:±234.
H β λ 4861	4981.6±2.0	0.02474±0.00040	7421.5±123.	25.1±13.	7.87:±4.	474.:±241.

Notes. The table lists: emission line centers, redshifts, line flux F in units of 10^{-15} erg s⁻¹ cm⁻², and line widths (FWHM) of the strongest emission lines.

Table A.6. S2 clean component.

Line	λ_{center} [Å]	z	v [km s ⁻¹]	F	$FWHM$ [Å]	$FWHM$ [km s ⁻¹]
[N II] λ 6583	6746.4±0.3	0.02476±0.00005	7427.3±14.	1063.±42.	15.94±0.64	709.±28.
H α λ 6563	6726.3±0.2	0.02491±0.00003	7473.9±9.	907.8.±27.	11.39±0.34	508.±15.
[N II] λ 6548	6709.4±0.5	0.02464±0.00007	7393.2±23.	469.6±19.	15.94±0.64	713.±28.
[O I] λ 6300	6452.2 ±0.5	0.02411±0.00008	7232.8±24.	209.3±10.	20.45±1.02	951.±47.
[O III] λ 5007	5131.0±1.0	0.02480±0.00019	7439.4±60.	54.3±5.	10.42±1.04	609.±61.
H β λ 4861	4977.2±2.0	0.02383±0.00041	7150.2±124.	20.0:±4.	8.29:±1.37	500.:±101.

Notes. The table lists: emission line centers, redshifts, line flux F in units of 10^{-15} erg s⁻¹ cm⁻², and line widths (FWHM) of the strongest emission lines.

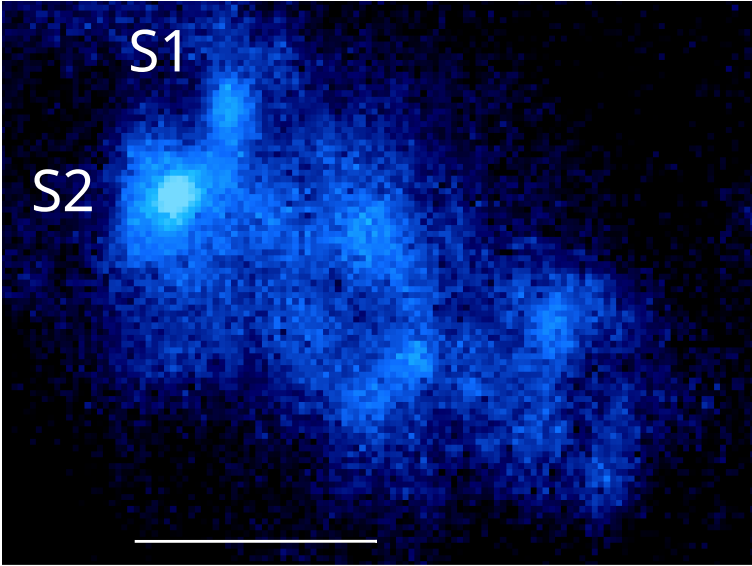


Fig. A.1. Enlarged [SII] image of the nuclei S1 and S2 and of the region southwest of the nuclei. North is to the top and east to the left. The white line is 1 arcsec long (same as Fig. 12).